Journal of Materials Science & Technology 144 (2023) 70–80

Contents lists available at ScienceDirect

Journal of Materials Science & Technology

journal homepage: www.elsevier.com/locate/jmst

Research Article

Annealing hardening effect aroused by solute segregation in gradient ultrafine-grained Mg-Gd-Zr alloy

Chunquan Liu[a,b,c], Xianhua Chen[a,b,*], Domonkos Tolnai[c], Yaobo Hu[a,b], Wei Zhang[d], Yusheng Zhang[d], Fusheng Pan[a,b]

[a] College of Materials Science and Engineering, Chongqing University, Chongqing 400045, China
[b] National Engineering Research Centre for Magnesium Alloys, Chongqing University, Chongqing 400045, China
[c] Institute of Metallic Biomaterials, Helmholtz-Zentrum Hereon, Max-Planck Street 1, Geesthacht 21502, Germany
[d] Northwest Institute for Nonferrous Metal Research, Xi'an 710016, China

ARTICLE INFO

Article history:
Received 8 September 2022
Revised 1 October 2022
Accepted 3 October 2022
Available online 28 November 2022

Keywords:
Ultrafine grains
Segregation
Annealing hardening

ABSTRACT

In this study, a remarkable annealing hardening effect was detected in gradient ultrafine-grained (UFG) Mg-0.32Gd-0.11Zr (at.%) alloy sheet fabricated by sliding friction treatment (SFT). Under the precipitation-free condition, the annealed UFG structure shows an obvious hardness increment from 1.40 GPa to 1.89 GPa after 200 °C heating for 12 h, which exhibits a much higher hardening response than the annealed coarse-grained (CG) structure. The high-angle annular dark-field scanning transmission electron microscopy (HAADF-STEM) and elemental mapping reveal prominent segregation of solute Gd atoms along grain boundaries, which endows the UFG structure with excellent grain boundary stability. Moreover, Gd segregation is also found around the extrinsic stacking fault (E-SFs) and the low-angle grain boundaries composed of edge dislocations. The large-scale solute partitioning provides a significant segregation hardening effect, which completely resists the softening effect aroused by the grain coarsening and dislocation annihilation. This work realizes a good combination of surface mechanical processing for fabricating UFGs and subsequent heat treatment, which earns desirable segregation hardening effects.

1. Introduction

Fabricating ultrafine grains (UFG) is an important and effective strengthening route in wrought Mg alloys [1,2]. In recent years, several surface mechanical treatment (SMT) methods such as surface mechanical attrition treatment (SMAT), friction stir processing (FSP), sliding friction treatment (SFT) were widely applied to manufacture the UFGs, which acquires significant grain boundary (GB) strengthening effect [3–5]. But such single improvement remains hard to meet the high requirement of the application in some engineering component areas. How to acquire abundant strengthening or hardening effects based on existing methods is still a research focus.

For most wrought Mg alloys that contain substantial amount of soluble alloying elements, heat treatment is an important procedure to adjust the microstructure and mechanical properties [6–8]. Besides the precipitation of secondary phase particles from the supersaturated solid solution matrix, scientists were increasingly concentrating on the segregation of solute atoms during the heat treatment, which is believed to affect many performances of metal alloys [9,10]. The notable segregation phenomenon is observed in Mg-Gd, Mg-Nd based alloy systems, etc. [11,12]. For example, Nie et al. found that the segregation of Gd atoms occurred in the tilt boundaries after annealing the cold deformed Mg-0.2Gd (at.%) alloy, which forms a range of unique, chemically ordered patterns [11,13]. Further, series segregation layers of alloy elements such as Nd, Mn, and Bi were observed at the broad interface of coherent $\{10\bar{1}0\}$ twin boundaries [12,14]. However, the existing researches mainly focus on the occupation of solute atoms in the matrix with careful atom scale. The influence of segregation on the performance of material, such as strength, GB stability, crystallographic texture, etc. lacks detailed analyses. As we know, crystal defects usually play an essential role in promoting the segregation of solute atoms and heterogeneous precipitation [15,16]. Therefore, it's reasonable to consider that the high density of defects including GBs, dislocations, and SFs created by SMT processing may arouse unpredictable hardening or softening effects as compared to the counterpart of coarse-grained (CG) structure.

* Corresponding author at: College of Materials Science and Engineering, Chongqing University, Chongqing 400045, China.
E-mail address: xhchen@cqu.edu.cn (X. Chen).

https://doi.org/10.1016/j.jmst.2022.10.015
1005-0302/

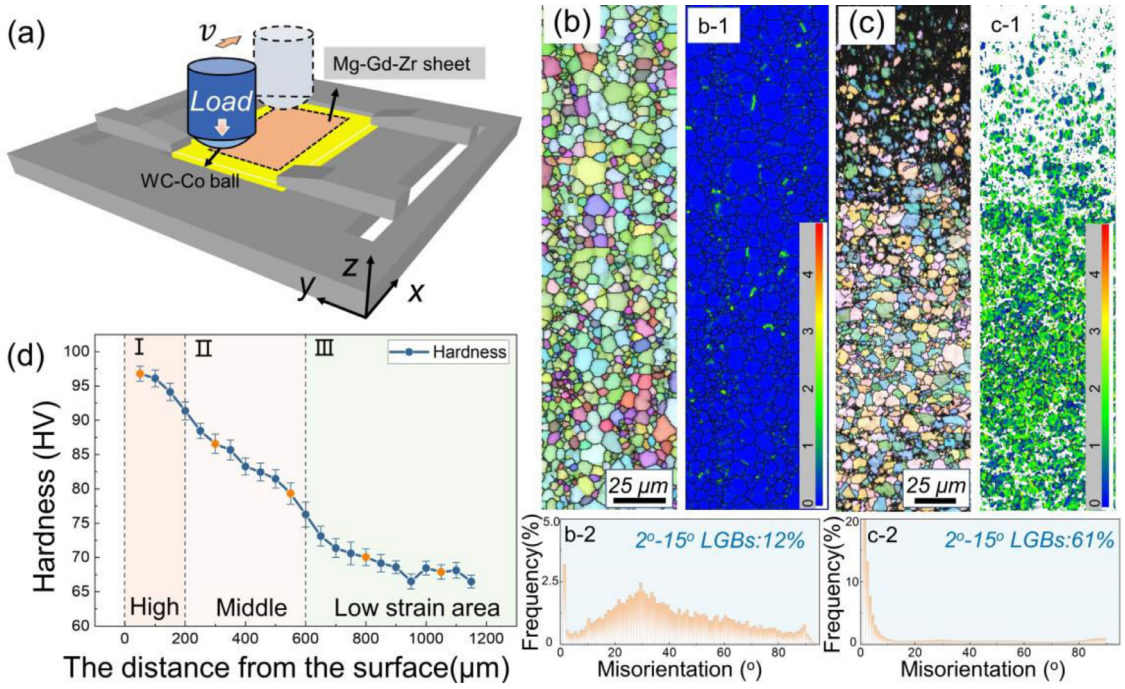

Fig. 1. (a) Schematic of the sliding fraction treatment (SFT); (b, c) The grain structure obtained by EBSD of the cross section before and after SFT; (b-1, c-1) corresponding kernel average misorientation (KAM) map; (b-2, c-2) corresponding misorientation angle distribution map; (d) The hardness distribution along the cross section of SFTed sample.

In order to realize a good combination of SMT technique and subsequent heat treatment, the restrictive relationship between the precipitation/segregation hardening and recovery softening should be emphasized [17,18]. Liu et al. found that the fast coarsening of UFGs and the annihilation of dislocations of SFTed Mg-Zn-RE alloy during the early aging stage cause a rapid softening effect, which largely offsets the hardening contribution of Mg-Zn-(RE) precipitations [2,19]. Hence, preventing or alleviating the coarsening of UFGs during the heat treatment is contributed to acquiring desirable hardening effect. Reiner considered that the enrichment of solute atoms at ubiquitous crystal defects is driven by the reduction of interfacial energy, so restricting grain growth and giving rise to stabilization of the systems [20]. Therefore, restricting the coarsening of UFG by inducing a big volume of solute segregations can not only alleviate the softening effect but also inspire the extra potential segregation hardening effect.

In the present work, an as-extruded Mg-0.32Gd-0.11Zr (at.%) was selected to fabricate the UFG structure by SFT technique and followed by annealing treatment under different temperatures. The segregation of Gd atoms at various defects such as GBs, dislocation array, and stacking faults were carefully investigated by high-angle annular dark-field (HAADF) scanning transmission electron microscope. The low content of Gd element (<1.5 at.%) can exclude the influence of the precipitation hardening, so giving a better evaluation about the segregation hardening effect. The aim of this work is to investigate the solute redistribution, GB stability, and the hardening mechanisms during the annealing treatment of SMT-processed Mg-Gd-Zr alloy.

2. Experimental procedures

2.1. Sliding friction treatment (SFT)

A specially designed ball-on-disk contact configuration was used to fabricate the ultrafine-grained structure on hot extruded Mg-0.32Gd-0.11Zr (at.%) alloy sheet, as shown in Fig. 1(a). A load was applied on the sheet which made the spherical WC–Co ball has a close contact with the sample surface. By the alternate sliding along x axis and the adjustment of y axis, a plastically deformed area was fabricated. The surface treatment was conducted under a constant load of 500 N with a friction velocity of 0.2 m/s. Detailed processes are presented in Refs [5,19].

2.2. Microstructure analysis

The microstructures were observed by using (i) a JEOL JSM-7800F field emission scanning electron microscope (SEM) equipped with a HKL Chanel 5 EBSD system, (ii) a transmission electron microscope (TEM) equipped with a high angle annular dark field (HAADF) detector with an accelerating voltage of 200 kV. After being mechanical ground and polished, the specimen for EBSD characterization was electropolished at −30 °C and 20 V for 60 s in electropolishing solution. Thin foil specimens for TEM observation were fabricated by mechanical polishing and ion-beam thinning using Gatan Precision Ion Polishing System at room temperature. The phase analysis was conducted by X-ray diffractometer (XRD, a Rigaku D/MAX-2500PC) using Cu-$K\alpha$ radiation with a scanning angle from 10° to 90° and a scanning speed of 2°/min. The dislocation density and lattice parameters were estimated using XRD line broadening analysis with the help of the Jade and Material analysis using diffraction (MAUD) software. Firstly, the crystallite size (D_c) and microstrain $\langle \varepsilon^2 \rangle^{1/2}$ were measured from the XRD patterns by MAUD. Then, the dislocation density can be estimated by:

$$\rho = \frac{2\sqrt{3}\langle \varepsilon^2 \rangle^{1/2}}{D_c b} \quad (1)$$

where b is the Burgers vector length. Corresponding detailed information of this method was presented before in Refs. [21–23]. The length measurement of grain size in the TEM and EBSD analyses was calculated by the software of Nano measurement.

2.3. Hardness test

The Vickers microhardness test on the cross-section was carried out using a Zwick tester at a constant load of 100 gf with a dwell time of 10 s. Each position was measured six times. After removing the maximum and minimum values, the average value of remaining four was taken as the microhardness of this position. In order to acquire reliable nanoindentation data, the surface of the test specimens was mechanically polished to mirror finishing. Quasi-static nanoindentation tests were performed at room temperature on a nano indenter (Agilent-G200) with a Berkovich diamond indenter. The sample surface was loaded at the strain rate ($\dot{\varepsilon}_L$) of 5 mN/s to the indentation depth of 2500 nm with a holding time of 5 s at maximum load.

3. Results

3.1. Microstructure

The original Mg-0.32Gd-0.11Zr (at.%) alloy sheet has an average grain size of 4.6 ± 2.2 μm, corresponding kernel average misorientation (KAM) map reflects the full dynamical recrystallization (DRX) occurred during hot extrusion [24], as shown in Fig. 1(b). After surface sliding friction treatment (SFT), the homogenous coarse-grained (CG) structure has been altered to a gradient structure. As compared with CG structure, the SFTed sample shows an obvious increment on local misorientation, and the account of low angle grain boundaries (LAGB) is increased from 12% to 61%, which is aroused by the large shear deformation during the alternate friction process [25]. Fig. 1(d) shows the micro-hardness profile along the cross-section of the SFTed sample. Due to the grain refinement and dislocation strengthening effect, the hardness close to the top surface reaches 97.2 ± 1.9 HV, and follows a gradually decreasing trend to the inner (67.1 ± 0.9 HV). Then, we compare the microstructure of the low strain CG area near 800 μm away from the surface and the high strain UFG layer close to top surface.

At the low strain layer of 800 μm away from the treated surface, although the grain size has not been obviously refined, the original full DRXed structure has been obviously altered to a deformed structure. In order to release the shear stress, as shown in Fig. 2(d), dislocations have been activated and accumulated, which accounts for the formation of low-angle grain boundaries within the grain. In addition, few secondary phase particles are detected in the HAADF-STEM image, corresponding mapping scanning results indicate the main elements are Gd and Zr, respectively. Generally, Zr cannot participate in the formation of intermetallic compounds, only acting as the heterogeneous nucleation sites to refine the grain size [26]. Previous studies reported that Gd can form Mg_x-Gd phases or Gd-containing hydrides [27]. Detailed identification will be conducted later.

Fig. 3 shows the TEM observation of the high strain area at a depth of ~ 50 μm from the surface. The microstructure is characterized by high density of ultrafine grains, which has an average grain size of 156 nm. Corresponding multi-continuous diffraction rings in the selected area electron diffraction (SADE) pattern illustrate that these UFGs are randomly oriented (the inset of Fig. 3(c)). SFT induces a kind of high-rate shear deformation on the surface layer and follows a gradient strain along the depth. Under the persistent accumulation of strain, a big volume of generated and multiplied dislocations can result in the formation of dislocation arrays, which gradually transform into substructures with minor misorientations and eventually evolve into stable grain boundaries (GBs) [25,28,29]. Finally, a gradient structure (GS) composed of UFG in the surface layer, submicron grain (SMG) in the middle and CG in the inner is fabricated on the alloy sheet. The grain refining process can be found in previous Refs. [19,25,29]. Meanwhile, a lot of residual defect structures also remain in the deformed high strain layer under the severe plastic deformation, as shown in Fig. 3(d) and (e). From the elemental scanning mappings of CG and UFG areas, there is no solute segregation phenomenon occurred prior to the annealing treatment.

3.2. Hardness evolution during different annealing temperatures

The hardness evolution of the gradient structure during the annealing treatment at 125 °C, 150 °C, 200 °C, and 275 °C is shown in Fig. 4. The UFG, SMG, and CG sample represents the area of near 50 μm, 300 μm, and 800 μm away from the surface, respectively. Under the low annealing temperature of 125 °C, the hardness of the cross-section exhibits a very small fluctuation with annealing time prolongs. But when the temperature goes to 150 °C, an obvious hardening effect emerges at UFG and SMG areas. In this condition, the biggest hardness increment (ΔH) of 12.9 ± 0.9 HV is located at UFG area, which reaches the peak point of 109.3 ± 2.1 HV after annealing about 44 h. When the temperature reaches 200 °C, the whole cross-section shows different ΔH. Among these three areas, the top UFG layer acquires the highest ΔH of 13.4 ± 0.8 HV after annealing 12 h. What's more, such hardness increment is gradually minimized with increasing distance to the treated surface. For example, the ΔH is only 3.7 ± 0.3 HV at the CG layer of 800 μm from the treated surface. When the temperature is set as 275 °C, the hardening effect is significantly weakened and even disappeared at the CG area. In addition, an obvious softening phenomenon is observed after reaching the peak point. Table 1 summarizes the ΔH value and the peak-time of the UFG layer and CG layer at different temperatures. Obviously, the elevating anneal temperature can shorten the time to reaching the peak hardness. What's more, the ΔH value is also affected by the temperature change, which shows a gradually increasing trend with the elevating temperature from 125 °C to 200 °C, but follows a decrease at the high annealing temperature of 275 °C.

By comparison, the best hardening effect is accomplished under the annealing temperature of 200 °C, which owns the highest ΔH value and a relatively short period of 12 h. In order to evaluate the hardening effect more carefully, further, nanoindentation test was conducted on UFG, SMG, and CG areas under this condition. Fig. 5 shows the load-displacement (*P-h*) curves of three areas before and after annealing treatment. Corresponding statistics of the values of hardness and the maximal load are summarized in Table 2. In agreement with Vickers hardness evolution, after SFT-processed, the hardness shows a gradually increasing trend from 0.876 GPa (CG) to 1.398 GPa (UFG). Corresponding needed max-load at a given indenter displacement of 2500 nm is increased from 125.9 mN (CG) to 187 mN (UFG), which reflects the obvious grain boundary hardening effect. After heat treatment, the hardness and needed max-load of three areas exhibit different increment further. Especially at the UFG area, the hardness improves from 1.398 GPa to 1.889 GPa, and the max-load increases from 187 mN (CG) to 235.3 mN, presenting the biggest hardening effect.

3.3. XRD analysis

Generally, precipitation strengthening aroused by the secondary phase particles during the heat treatment is regarded as the main mechanism to strengthen the wrought Mg alloys, especially in RE-containing alloys [30,31]. For example, Gao et al. investigated the microstructure evolution in a Mg-15Gd-0.5Zr (wt.%) alloy during isothermal aging treatment at 250 °C, which found that the precipitation of prismatic β' plates can provide a remarkable hardening effect [32]. In this work, the hardness of the gradient structure has various ΔH values at different annealing temperatures. But

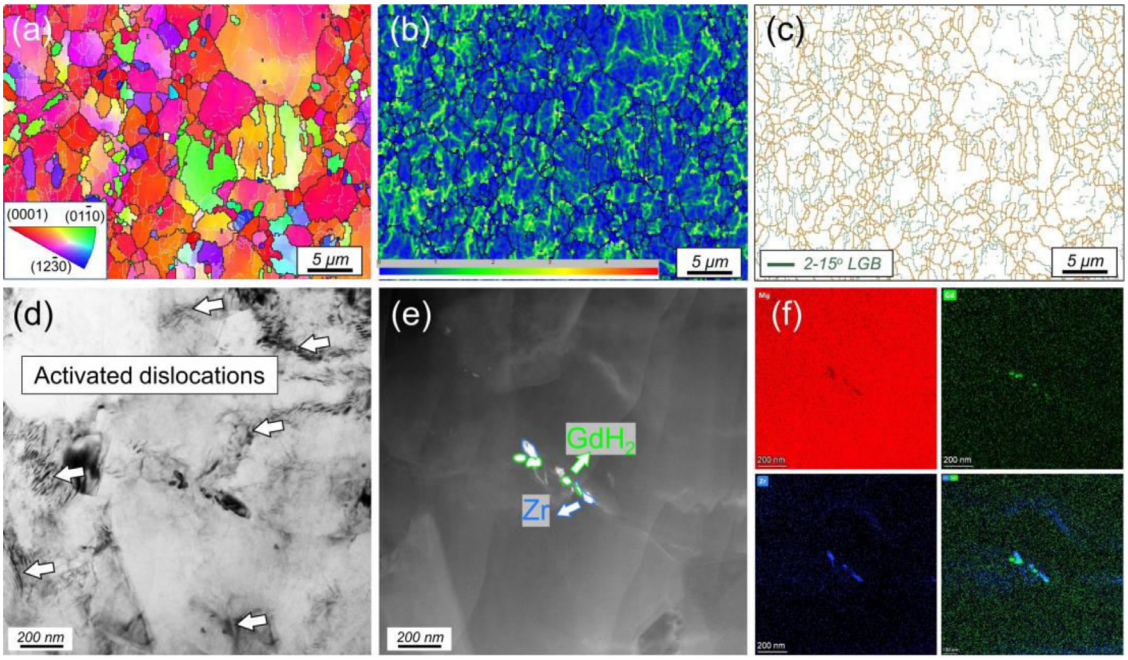

Fig. 2. EBSD micrographs and TEM observations of the low strain layer of 800 μm away from the treated surface. (a) Inverse pole figure map; (b, c) corresponding KAM map and the distribution of low-grain boundaries map; (d) bright field TEM image; (e, f) corresponding HAADF-STEM image and elemental mapping analyses.

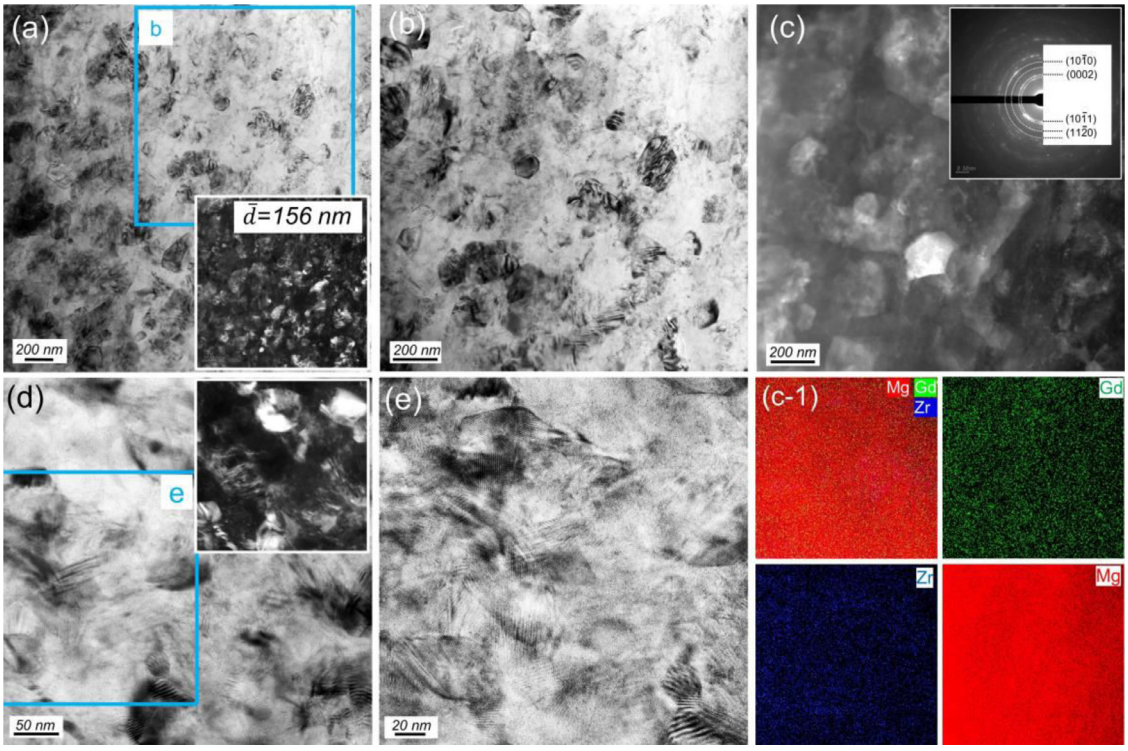

Fig. 3. (a, b) Bright and dark TEM observations of the high strain area near 50 μm from the surface; (c, c-1) HAADF-STEM image and corresponding elemental mapping analyses; (d) the dislocation activities within the UFGs; (e) high-resolution image of the blue frame f in (d).

Table 1
The hardness increment (ΔH) and the time of reaching peak point (Time-P) at different areas under different temperatures (125 °C, 150 °C, 200 °C, 275 °C).

Temp.	125 °C		150 °C		200 °C		275 °C	
Area	UFG	CG	UFG	CG	UFG	CG	UFG	CG
ΔH	0.9±0.3	/	12.9±0.9	0.3±0.1	13.4±0.8	3.7±0.3	6.6±0.4	/
Time-P	48 h	/	44 h	56 h	12 h	12 h	6 h	/

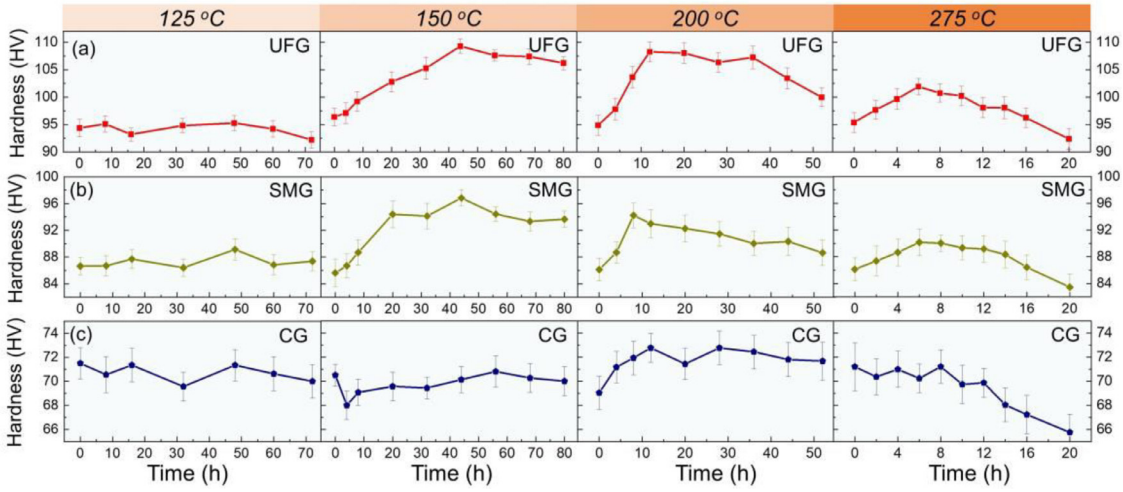

Fig. 4. The Vickers hardness evolution of different areas under anneal temperatures from 125 °C to 275 °C. (a) the UFG layer near 50 μm from the surface; (b) the SMG layer near 300 μm from the surface; (c) the CG layer near 800 μm from the surface.

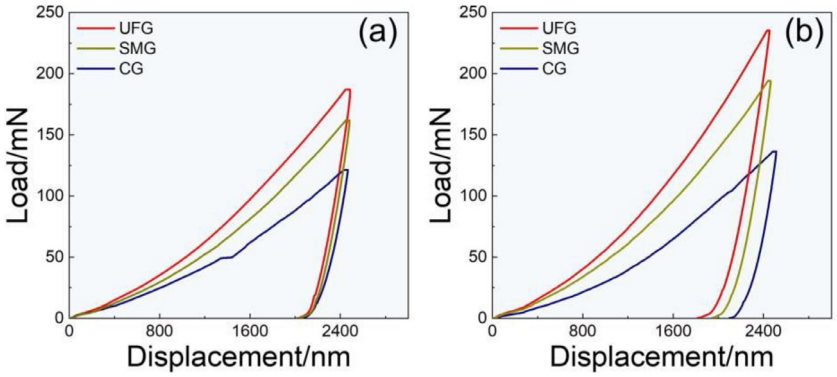

Fig. 5. Load-displacement (P–h) curves of UFG, SMG and CG areas. (a) Before annealing treatment; (b) after annealing for 12 h under 200 °C.

Table 2
The hardness, maximal load of the CG, SMG and UFG areas from the nanoindentation test.

	CG		SMG		UFG	
	0 h	12 h	0 h	12 h	0 h	12 h
Hardness/GPa	0.88	0.96	1.19	1.48	1.40	1.89
Max. load (mN)	125.9	136.4	161.8	194.1	187	235.3

the present alloy system almost exhibits a character of secondary phase free due to the low alloying contents, as shown in the previous TEM observations. Corresponding XRD patterns also reveal that there are no diffraction peaks for any other precipitations besides the α-Mg phase. But the XRD patterns from 30° to 40° shows that the α-Mg diffraction peaks migrate to larger angle during the annealing process, as seen in Fig. 6(b, e). This phenomenon may be attributed to the decomposition of the α-Mg solid solution, which will result in the reduction of lattice parameters [21]. Therefore, it is reasonable to deduce that the annealing treatment would arouse the migration and diffusion of solute atoms, so producing another hardening effect. On the other side, the peak intensity of three typical crystal planes of (001), (002), and (101) exhibits no obvious change during the heating, reflecting that the grain orientation has not been affected [33]. The dislocation density, crystallite size and lattice constants' ratio c/a of CG and UFG areas after annealing 0 h, 12 h, and 50 h are shown in Fig. 6(c,f). The crystallite size of UFG layer exhibits a good resisting ability for coarsening, which agrees well with the limited grain growth observed in the following TEM observations (Fig. 7). The dislocation density in CG and UFG areas decreases with prolonged annealing time. Moreover, the lattice parameter ratio (c/a value) of CG sample is increased with annealing time, revealing that the lattice distortion is gradually minimized due to the migration of solute atoms [15,34].

4. Discussion

4.1. Segregation of solute atoms

In order to reveal the influence of heat treatment on microstructural evolution, the TEM observations at the area of 50 μm away from the surface after annealing 12 h are conducted, as shown in Fig. 7. Generally, heat treatment always makes the grain enlarged. Interestingly, the coarsening of grain size at present condition is insignificant, just increased from 156 nm to 184 nm. In addition, the residual dislocations aroused by SFT have been annihilated largely, presenting as the almost clean strain-free grains. Some cuboid precipitates, with dimensions of ~50 nm, are observed in the HAADF-STEM image. The SAED patterns are matched well with GdH_2 phase, which is one of RE hydrides with face-centered cubic (fcc, a = 0.53 nm) structure [27]. This RE hydride is formed as a result of the decomposition of Mg-RE intermetallic phases by hydrogen during solidification or high-temperature heat treatment [27,35]. Importantly, it is clear to figure out the grain boundaries by the bright white network. At the model of HAADF-STEM observation, Z (atomic number)-contrast can be distinguished due to the differences of atomic numbers (Mg: 12,

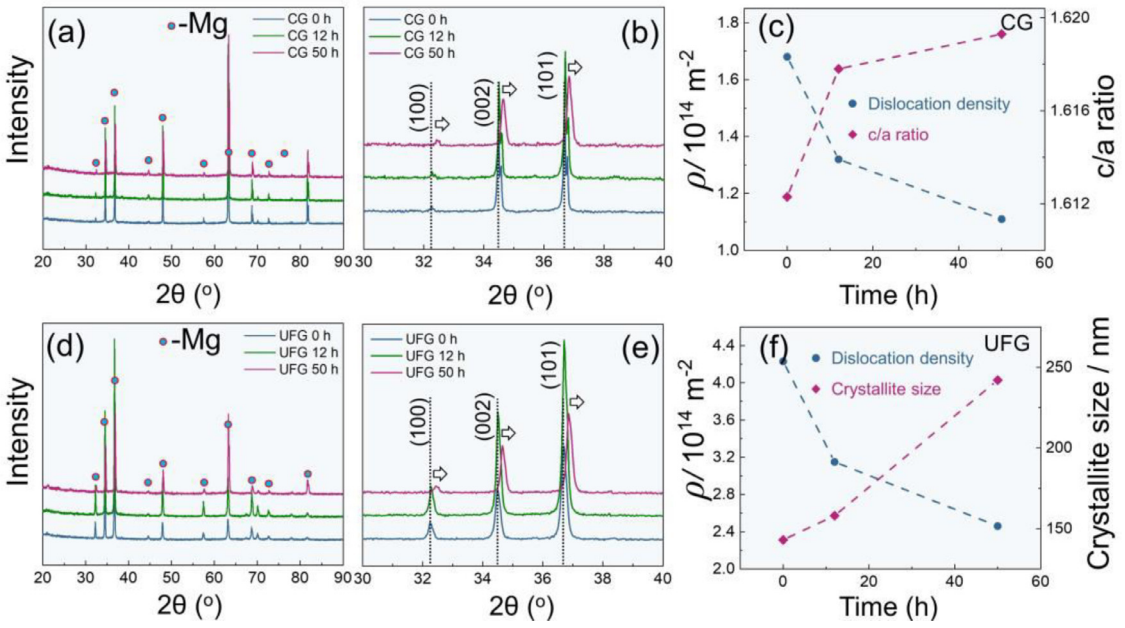

Fig. 6. (a, d) Overview of XRD patterns of the CG layer and UFG layer annealed under 200 °C with 0 h, 12 h and 50 h, respectively; (b, e) enlarged section of the XRD patterns; (c, f) dislocation density, crystallite size and lattice axial ratio *c*/*a* statistics at different conditions.

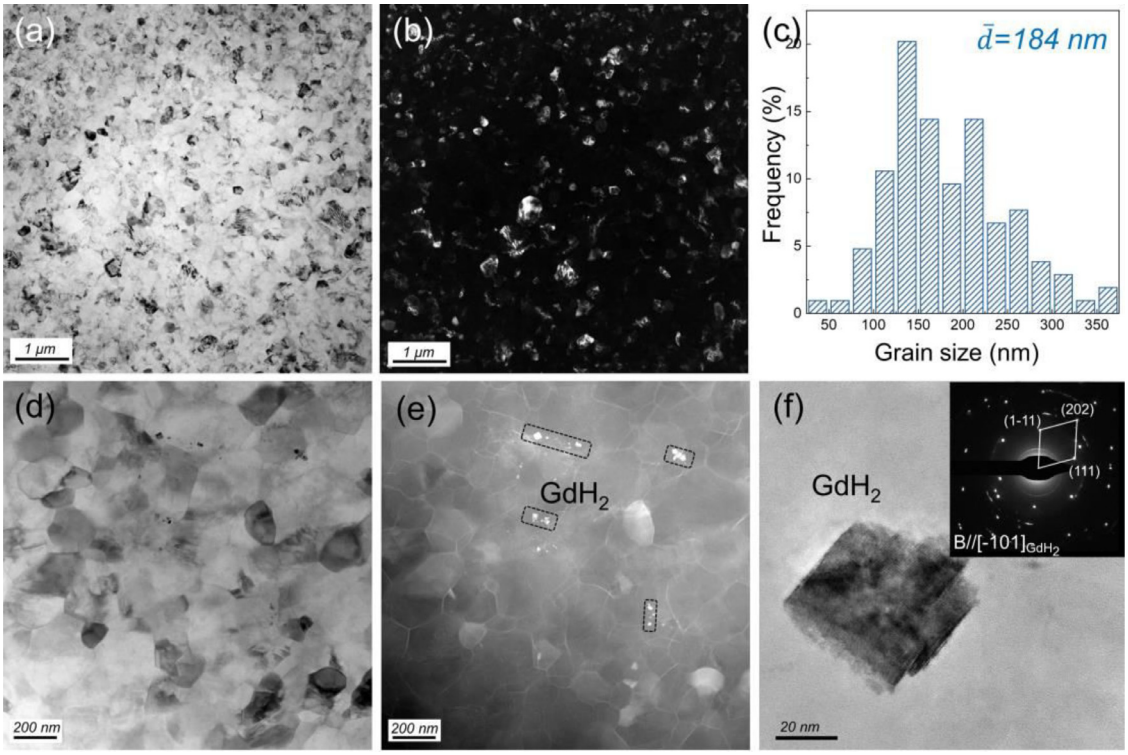

Fig. 7. (a, b) The bright and dark field images of the area near 50 μm from the surface after 200 °C heating 12 h; (c) the grain size distribution map; (d, e) enlarged TEM and HAADF-STEM image; (f) TEM micrograph of the secondary phase and corresponding SAED patters.

Zr: 40, Gd: 64), characterized by different light and shade contrast [36]. Therefore, the atomic segregation occurred indeed during the annealing treatment. Further, the detailed segregation phenomenon is analyzed.

As shown in Fig. 8(b), an obvious atomic segregation with a width near 5 nm is characterized along grain boundaries, corresponding EDS mapping analyses reveal the enrich element is Gd element. Besides the GB segregation, the same bright white enrich areas are also found within the UFGs, marked as the yellow arrows in the HAADF-STEM and EDS maps. Further, the high-resolution image indicates that a lot of dislocation are located at the end of the extra lattice planes within the grain. The matrix has been divided into two subgrains misoriented by 3.6° by these dislocation arrays, and corresponding Fourier transform patterns is shown in the inset of Fig. 8(d). According to the related EDS scanning results, the LAGBs containing abundant edge dislocations also exhibit the Gd segregation phenomenon. In order to evaluate the micro-strain distribution around the segregation area, the geo-

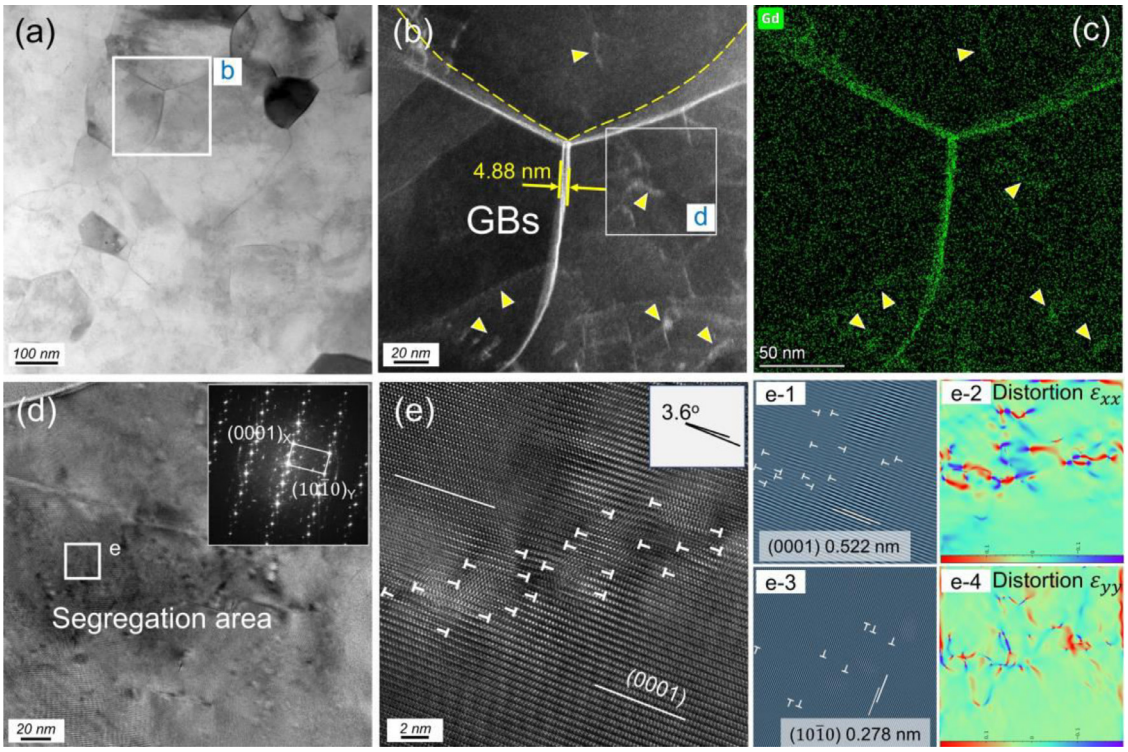

Fig. 8. (a, b) The bright field TEM image and HAADF-STEM image of segregated UFGs; (c) corresponding EDS-mapping analyses; (d, e) further high-resolution TEM observation within the UFGs, the inset in (d) is Fourier transform patterns of (e); (e-1, e-3) inverse FFT images obtained from {0001} and {10$\bar{1}$0} reflection, respectively, in which dislocation cores are marked as white symbol "⊥"; (e-2, e-4) corresponding GPA distortion maps of {0001} and {10$\bar{1}$0} planes.

metric phase analysis (GPA) method is adopted because it is sensitive to minor displacements of lattice fringes. This method has been used previously in the analysis of inner defects such as dislocations or low-angle tilt boundaries [12,13,37]. For example, Kou et al. well-illustrated the process of a dislocation impinging into a twin-twin intersection by using GPA analyses and found an unusual pathway for dislocations [37,38]. Fig. 8(e-1) to (e-4) reveal the inverse fast Fourier transform (IFFT) image and corresponding distortion GPA maps of (0001) and (10$\bar{1}$0) planes, respectively. The distortion maxima (near ±0.1) are located at the dislocation cores and their positions are consistent with those in the IFFT image. Generally, as compared with the heavily deformed state, annealing treatment can make the most of implanted dislocations annihilate so alleviating the lattice distortion aroused by large shear strain. Meanwhile, solute atoms tend to migrate toward the dislocation under the stress field during the heat treatment process [39]. Nie et al. considered that the solute atoms with a larger radius than that of Mg (1.595 Å), such as the Gd (1.822 Å) in the present study, tend to migrate to the extension region of the dislocation core [11,40]. On the contrary, the solute atoms with a smaller radius will occupy the compression region of the dislocation core. Such transfers of solute atoms are beneficial for reducing the elastic strain energy, so improving the stability of the whole system. Finally, the segregation occurs at these dislocation-rich areas and impedes their annihilation simultaneously, arousing the obvious lattice distortion.

Besides the dislocation, stacking faults is also regarded as a common defect in deformed metals. As shown in Fig. 9(a–d), the stacking faults are found within the segregated UFGs, corresponding EDS scanning results reveal an obvious Gd segregation phenomenon, marked by green arrows. HRTEM results show that the stacking sequence follows "…ABABCAB…", which is known as an extrinsic stacking fault (E-SFs) in the hcp structure [41]. As compared with the standard stacking sequence of "…ABABAB…" in Mg alloys (Fig. 9(e-2)), E-SFs is simply achieved by inserting a section of "C" plane into the hcp structure. Suzuki considered that chemical interactions in metal alloys would induce the segregation of solute atoms to stacking faults, which is called "Suzuki segregation" or "Suzuki effect"[42]. Recent years, Suzuki segregation was observed in Cu-Si, Co-Ni-based superalloys as well as Mg-Zn-Y alloys etc. [42,43]. These reported segregation phenomena around SFs are mainly realized by (i) hot plastic deformation or (ii) aging treatment after cold deformation. In this work, SFT technique is conducted at ambient temperature, the heat rise aroused by sliding process is limited and that is hard to cause the diffusion of atoms [25]. But intense shear strain has allowed many defects existed in these newly generated UFGs, such as dislocations and stacking faults, which provide energetically preferable conditions for segregation in the followed annealing treatment and eventually result in the Suzuki effect [40,44].

In order to have a comparison with UFG area, the segregation phenomenon at the CG layer of 800 μm away from the top surface is also characterized. Although the hardness increment ΔH is limited at this area, the segregation of Gd element along grain boundaries is also existed, as shown in Fig. 10(c). After annealing treatment for 12 h, the distortion-free maps analyzed by GPA method reveal that the residual dislocations within the grain aroused by SFT have largely been annihilated. Besides the segregation along grain boundaries, there is no obvious elemental segregation found in the grain interior. Therefore, the annihilation of dislocation and the segregation of solutes are simultaneously occurred during the heat treatment.

Generally, the interface with higher interfacial energy (Γ) owns higher possibilities for interfacial segregation. Normally, the interfacial energy in Mg alloys usually follows the sequence of $\Gamma^{\text{High-GB}} > \Gamma^{\text{Low-GB}} > \Gamma^{\text{SF}}$ [11,44,45]. So, the stable HAGB becomes the most favorable and common site for the segregation of impurities and solutes. But in present study, the solute atoms (Gd) have

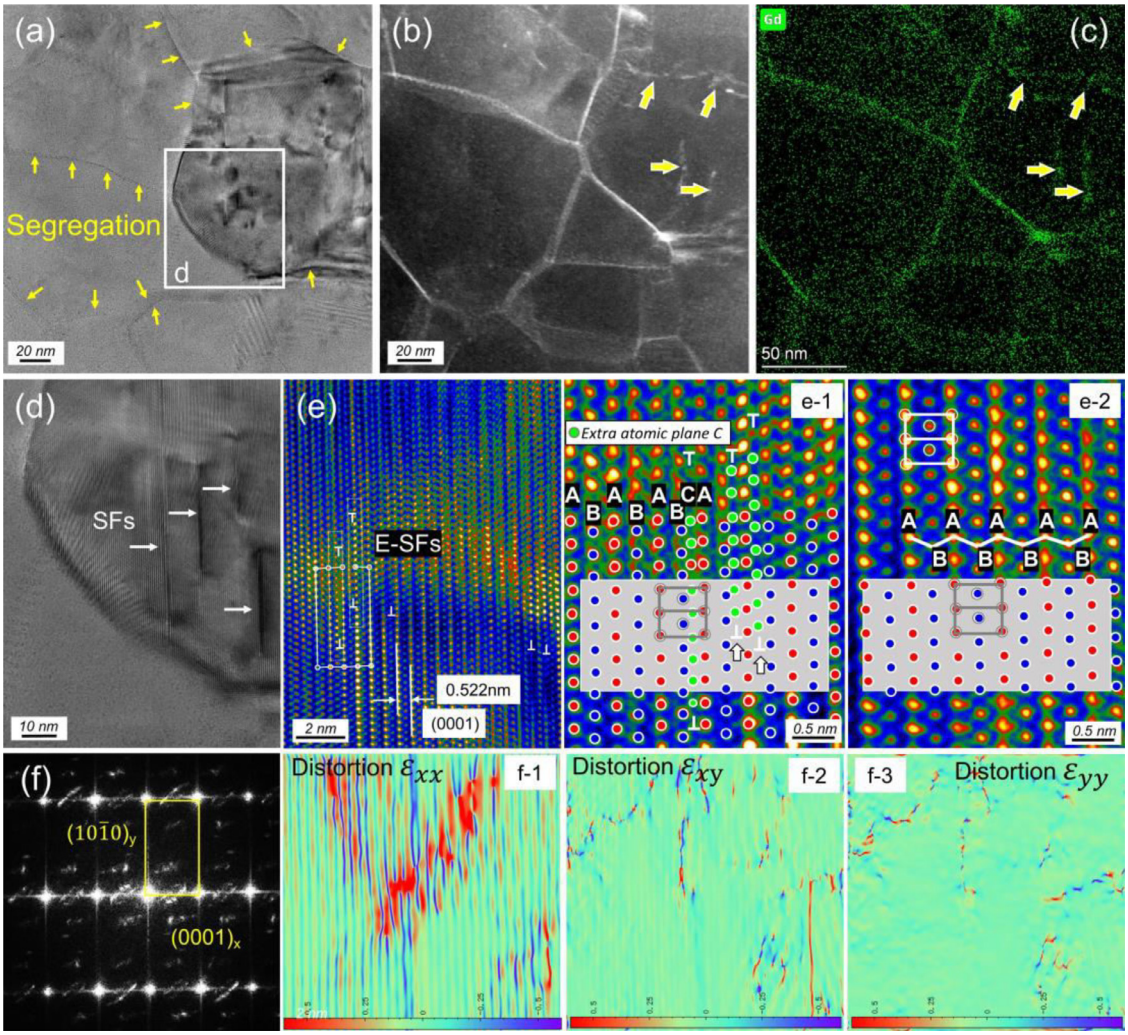

Fig. 9. (a–c) TEM, HAADF-STEM and EDS-scanning images of UFGs; (d, e) The high-resolution (HR) TEM image of stacking faults within the grain; (e-1, e-2) the comparison of atomic arrangement of SFs-containing area and SFs-free area; (f) FFT pattern and corresponding GPA analyses of SFs-containing region.

segregated simultaneously both around the HAGBs, LAGBs as well as the stacking faults, which is rarely reported in Mg alloys. It's reasonable to consider that the unusual annealing hardening effect would be attributed to the extraordinary migration of solute atoms. A detailed discussion will be seen in next part.

4.2. Hardening effect aroused by segregation

In a word, we successfully realize the good combination of SMT process and subsequent heat treatment that earns desirable hardening effects. As compared with the original CG structure, the hardness of annealed UFG layer receives more than twice increment. But this optimal improvement of hardness is accomplished under the mutual competition from various aspects, such as the hardening effect from segregation and the softening effect from dislocation annihilation or grain coarsening, etc. [46]. Next, we will discuss the multiple mechanisms which are thought to contribute to the explanation of hardness evolution.

Firstly, the GBs hardening can be explained by the Hall-Petch model, which presents as [2,21]:

$$\Delta \mathrm{HV}_{\mathrm{GB}} = C k_{\mathrm{hp}} d^{-1/2} \tag{2}$$

where C is a constant, k_{hp} is the Hall-Petch constant for Mg polycrystals, d is the grain size. As we know, grain size gives large influence on the elastic and plastic deformation of metal metals, mainly reflecting as the activation of dislocation and twins [5]. A well-controlled grain size can realize desirable mechanical properties. In the present study, in order to acquire a satisfying hardening effect, preventing the excessive grain coarsening is important. As shown in Fig. 6, after annealing for 12 h at 200 °C, the grain size only increases from 156 nm to 184 nm. The excellent grain size stability is attributed to the segregation of Gd atoms along the GBs. It's well known that grain boundaries are in a metastable thermodynamic equilibrium in the presence of solute atoms [47,48]. The partitioning of solute atoms can reduce the total Gibbs free energy, G, thus giving rise to stabilization of all crystalline defects, such as GBs and dislocations [49–51]. Due to the limited grain coarsening effect, the GB strengthening only exhibits a small decrement after heat treatment, which provides a solid foundation for the hardening of UFG areas.

The mutual interaction of dislocations hinders their motion. The increase or decrease of dislocation density thus leads to the hardness alternation, which can use the existing models (see e.g. Refs. [1,23]):

$$\Delta \mathrm{HV}_{\mathrm{d}} = CM\alpha_1 Gb\sqrt{\rho} \tag{3}$$

where M is the Taylor factor; α_1 is a constant; G is the shear modulus, b is the length of the Burgers vector; ρ is the dislocation density. As shown in previous TEM and XRD analyses, the residual dislocations aroused by SFT have been annihilated largely, corre-

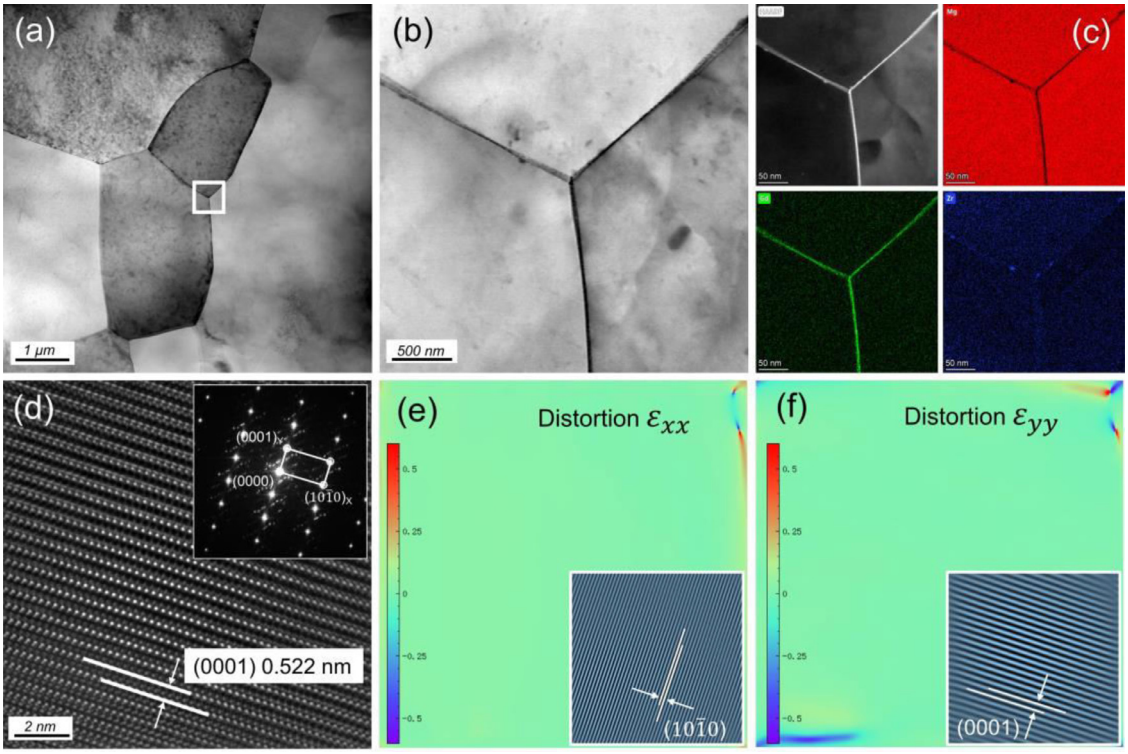

Fig. 10. (a, b) Bright TEM image at the low strain layer of 800 μm away from the treated surface after 200 °C annealing 12 h, (b) is magnified image of white frame in (a); (c) HAADF-STEM image and corresponding EDS scanning results of (b); (d) High-resolution TEM observation within the coarse grain; (e–f) corresponding GPA distortion maps of {0001} and {10–10} planes.

sponding dislocation density is decreased from 4.23×10^{-14} m^{-2} to 2.46×10^{-14} m^{-2}, which brings a decreasing dislocation hardening.

For solid solution hardening, the contribution in the present alloy system can be estimated using the following formula [52]:

$$\Delta HV_{ss} = Ck_{Gd} \times x_{Gd}^{2/3} \quad (4)$$

where k_{Gd} is a constant for element Gd (1168 MPa (at.%)$^{-2/3}$ [53] and x_{Gd} is the atomic fraction of solute Gd element for the matrix, which is measured using STEM-EDS analyses. Zr element is ignored here because of the low solute ability. For the SFT-processed sample, the concentration is detected as 0.23±0.04 at.% Gd, while after annealing treatment, it reduces to 0.12±0.07 at.% Gd. The partitioning of solute atoms arouses a decreasing solid solution hardening.

Besides above-mentioned hardening effects, the precipitation hardening is another important method, especially in Mg-RE alloy systems. Generally, the secondary phase particles can impede the movement of dislocations so that improving the hardness or strength of metals. According to the Oroawan-Ashby mechanism, the hardness increment can be approximated by [2,21,22]:

$$\Delta HV_{vp} = C\frac{0.13Gb}{\lambda}\ln\frac{d_p}{2b} \quad (5)$$

where d_p is the average diameter of the precipitates, and λ is the mean planar inter-partical spacing. But the present alloy system exhibits an almost precipitation-free condition both before and after heat treatment in previous TEM observations. Only a few GdH_2 phases with small size are detected. Therefore, the precipitation hardening effect is limited and ignored in this study.

From the contribution change of the above regular strengthening mechanisms, the annealing treatment brings an obvious softening effect on the UFG layer. However, the UFG layer still acquires a considerable ΔH of 0.5 GPa, which reveals a significant segregation hardening effect. What's more, interestingly, although the segregation phenomenon is also detected in the counterpart of CG area, theΔH is only 0.08 GPa. As compared with CG area, the characteristic of solute segregation in the UFG area are mainly reflected as two points. Firstly, due to the significant grain refining aroused by SFT processing, the density of the GBs containing the solute segregation at unit area is much higher. During the loading period, the dislocations have been activated and move along slip plans towards GBs under external stress, which causes the stress concentration [54]. The big volume of segregation along GBs will impede the moving of dislocations. Therefore, the strength is improved due to the additional external load to accomplish the increase in free energy related to disruption of these near neighbor bond between solute atoms. Secondly, besides the GB segregation, the UFG area contains the dislocation and SF segregation which does not existed in the CG area. Under the heating process, the low density of defect structure at the CG inner has been fast annihilated, which cannot arouse the formation of dislocation and Suzuki segregation. Therefore, the insufficient volume of segregation cannot provide an effective hardening effect. However, the SMG area owns a moderate hardness increment, as shown in Table 2. This is because (i) the GBs density of SMG area is between that of UFG and CG areas; (ii) the SMG area contains a big volume of defect structures that have not been transformed into stable GBs. These residual defects can also arouse the segregation like LAGBs and SFs segregation so improving the hardness [13,42]. Therefore, the excellent hardening effect is benefited from the defect structure generated by SFT and the segregation along defects caused by heat treatment, both of which are indispensable. But it's worth to mention that although the high density of defects has been implanted in the GS structure which can promote the segregation hardening, the hardness improvement is also restricted by the softening effect aroused by dislocation annihilation. As shown in Fig. 6(c, f), the decrease of dislocation density of the UFG area is more severe than that of the

CG area. Therefore, the hardness in UFG and SMG areas shows a sluggish increment similar to the CG area.

Under the effect of segregation hardening, the UFG, SMG, and CG areas acquire different ΔH values at different annealing temperatures from 150 °C to 275 °C, which means that the temperature has a large influence on the hardness evolution. On one side, high temperature is not beneficial for the metal to keep good GB stability [20]. In addition, the annihilation of dislocation will be accelerated at a high temperature. When the segregation hardening effect cannot compensate for these softening effects, the hardness will drop after reaching the peak point. Especially under the high annealing temperatures of 200 °C and 275 °C, the softening effect gets more obvious, as shown in Fig. 4. On the other hand, the diffusion and migration of solute atoms are closely related to temperature too. The diffusion coefficient (D) can be predicted by the following form [55,56]:

$$D = D_0 \exp\left[-\frac{Q}{RT}\right] \tag{6}$$

where D_0 is the pre-exponential coefficient that includes the jump frequency, Q is the activation energy, T is the temperature, and R is a constant. Therefore, the higher temperature can improve the diffusion of solute atoms and arouse effective segregation along defects. More prominent solute segregation will arouse more hardening effects. But higher temperature also accelerates the annihilation of dislocation, which brings a soft effect. Under two race conditions, therefore, the sample annealed at 150 °C exhibits similar peak hardness as compared with the condition of 200 °C. What's more, the time for reaching the peak hardness is reduced after arising the annealing temperature, which is also influenced by the improved diffusion coefficient.

5. Conclusions

In this work, the ultrafine-grained Mg-0.32Gd-0.11Zr (at.%) alloy sheet processed by SFT was subjected to subsequent annealing treatment. The microstructure of UFG and the counterpart of CG structure before and after annealing were investigated systematically. The key findings are summarized as follows:

(1) Through the combination of SFT technique and annealing treatment at 200 °C for 12 h, the hardness of annealed UFG structure increases from 1.40 GPa to 1.89 GPa under the precipitation-free condition, which exhibits a more desirable hardening response than that of the annealed CG structure, from 0.88 GPa to 0.96 GPa.
(2) The thermal stability of UFG structure is improved by the segregation of Gd atoms along grain boundaries, so preventing the excessive growth of grain size during the annealing treatment.
(3) The Gd segregation is found around the HAGBs, LAGBs, and extrinsic stacking faults (E-SFs) simultaneously. The big volume of solute segregation provides a prominent hardening effect, which completely resists the softening effect aroused by the grain coarsening and dislocation annihilation.

Declaration of Competing Interest

The authors declare that they have no known competing financial interests or personal relationships that could have appeared to influence the work reported in this paper.

Acknowledgments

This work was financially supported by the National Natural Science Foundation of China (Nos. 52225101 and 52171103), the National Key R&D Program of China (No. 2021YFB3701100), the Fundamental Research Funds for the Central Universities (No. 2020CDJDPT001), the Natural Science Basic Research Plan in Shaanxi Province of China (No. 2022JM-233). The author would like to thank the Joint Lab for Electron Microscopy of Chongqing University. Chunquan Liu is grateful for financial support from the Chinese Scholarship Council (CSC No. 202106050087).

References

[1] W. Sun, B. Wu, H. Fu, X.-S. Yang, X. Qiao, M. Zheng, Y. He, J. Lu, S.-Q. Shi, J. Mater. Sci. Technol. 99 (2022) 223–238.
[2] C. Liu, X. Chen, Y. Yuan, W. Zhang, Y. Zhang, F. Pan, J. Mater. Sci. Technol. 78 (2021) 20–29.
[3] X.Y. Shi, Y. Liu, D.J. Li, B. Chen, X.Q. Zeng, J. Lu, W.J. Ding, Mater. Sci. Eng. A 630 (2015) 146–154.
[4] M. Gao, I.P. Etim, K. Yang, L. Tan, Z. Ma, Mater. Sci. Eng. A 829 (2022) 142058.
[5] C. Liu, X. Chen, W. Zhang, Y. Zhang, F. Pan, Mater. Sci. Eng. A 776 (2020) 138995.
[6] J.S. Suh, B.-C. Suh, S.E. Lee, J.H. Bae, B.G. Moon, J. Mater. Sci. Technol. 107 (2022) 52–63.
[7] X. Peng, W. Liu, G. Wu, H. Ji, W. Ding, J. Mater. Sci. Technol. 99 (2022) 193–206.
[8] Q. Li, X. Peng, F. Pan, J. Magnes. Alloy. 9 (2021) 2223–2224.
[9] H. Zhou, G.M. Cheng, X.L. Ma, W.Z. Xu, S.N. Mathaudhu, Q.D. Wang, Y.T. Zhu, Acta Mater. 95 (2015) 20–29.
[10] Z.L. Chao, Z.W. Wang, L.T. Jiang, S.P. Chen, B.J. Pang, R.W. Zhang, S.Q. Du, G.Q. Chen, Q. Zhang, G.H. Wu, Mater. Des. 215 (2022) 110449.
[11] Y.M. Zhu, S.W. Xu, J.F. Nie, Acta Mater. 143 (2018) 1–12.
[12] H. Xie, H. Pan, J. Bai, D. Xie, P. Yang, S. Li, J. Jin, Q. Huang, Y. Ren, G. Qin, Nano Lett. 21 (2021) 9642–9650.
[13] Y.M. Zhu, M.Z. Bian, J.F. Nie, Acta Mater. 127 (2017) 505–518.
[14] X. Zhao, H. Chen, N. Wilson, Q. Liu, J.F. Nie, Nat. Commun. 10 (2019) 3243.
[15] M. Bugnet, A. Kula, M. Niewczas, G.A. Botton, Acta Mater. 79 (2014) 66–73.
[16] D.F. Shi, C.M. Cepeda-Jiménez, M.T. Pérez-Prado, J. Magnes. Alloy. 10 (2022) 224–238.
[17] W.T. Sun, X.G. Qiao, M.Y. Zheng, X.J. Zhao, H.W. Chen, N. Gao, M.J. Starink, Scr. Mater. 155 (2018) 21–25.
[18] Q. Luo, Y. Guo, B. Liu, Y. Feng, J. Zhang, Q. Li, K. Chou, J. Mater. Sci. Technol. 44 (2020) 171–190.
[19] C. Liu, X. Chen, W. Zhang, Y. Zhang, F. Pan, Mater. Charact. 166 (2020) 110423.
[20] R. Kirchheim, Acta Mater. 50 (2002) 413–419.
[21] W.T. Sun, X.G. Qiao, M.Y. Zheng, C. Xu, S. Kamado, X.J. Zhao, H.W. Chen, N. Gao, M.J. Starink, Acta Mater. 151 (2018) 260–270.
[22] M.Y. Murashkin, I. Sabirov, A.E. Medvedev, N.A. Enikeev, W. Lefebvre, R.Z. Valiev, X. Sauvage, Mater. Des. 90 (2016) 433–442.
[23] W.T. Sun, X.G. Qiao, M.Y. Zheng, C. Xu, N. Gao, M.J. Starink, Mater. Des. 135 (2017) 366–376.
[24] B.-J. Lv, S. Wang, T.-W. Xu, F. Guo, J. Magnes. Alloy. 9 (2021) 840–852.
[25] W. Zhang, J. Lu, W. Huo, Y. Zhang, Q. Wei, Philos. Mag. 98 (2018) 1576–1593.
[26] Q. Zhang, H. Pang, Q. Li, Y. Gui, X. Chen, X. Li, P. Chen, J. Tan, Mater. Sci. Eng. A 835 (2022) 142679.
[27] R. Alizadeh, R. Mahmudi, A.H.W. Ngan, P.H.R. Pereira, Y. Huang, T.G. Langdon, Metall. Mater. Trans. A 47 (2016) 6056–6069.
[28] K. Liu, S.S. Nene, M. Frank, S. Sinha, R.S. Mishra, Appl. Mater. Today 15 (2019) 525–530.
[29] W. Zhang, Q. Wei, W.T. Huo, J.W. Lu, J.J. Hu, Y.S. Zhang, Vacuum 143 (2017) 236–240.
[30] S. Liu, H. Liu, X. Chen, G. Huang, Q. Zou, A. Tang, B. Jiang, Y. Zhu, F. Pan, J. Mater. Sci. Technol. 113 (2022) 271–286.
[31] D. Zhang, J. Zhang, Y. Zhang, D. Zhang, T. Xu, B. Li, Y. Zhao, J. Meng, Mater. Sci. Eng. A 854 (2022) 143791.
[32] X. Gao, S.M. He, X.Q. Zeng, L.M. Peng, W.J. Ding, J.F. Nie, Mater. Sci. Eng. A 431 (2006) 322–327.
[33] J.P. Hadorn, T.T. Sasaki, T. Nakata, T. Ohkubo, S. Kamado, K. Hono, Scr. Mater. 93 (2014) 28–31.
[34] R. Pei, Y. Zou, D. Wei, T. Al-Samman, Acta Mater. 208 (2021) 116749.
[35] D. Zhao, X. Chen, J. Ye, T. Chen, Y. Dai, C. Liu, Z. Luo, S. Gao, J. Zhang, J. Yao, A. Atrens, A. Tang, F. Pan, J. Alloys Compd. 810 (2019) 425–435.
[36] Y. Zheng, Y. Liu, N. Wilson, S. Liu, X. Zhao, H. Chen, J. Li, Z. Zheng, L. Bourgeois, J.-F. Nie, Acta Mater. 184 (2020) 17–29.
[37] Z. Kou, R. Huang, Y. Yang, T. Feng, S. Tang, S. Lan, L. Yang, Scr. Mater. 221 (2022) 114956.
[38] Z. Kou, T. Feng, S. Lan, S. Tang, L. Yang, Y. Yang, G. Wilde, Nano Lett. 22 (2022) 6229–6234.
[39] X.-F. Gu, T. Furuhara, L. Chen, P. Yang, Scr. Mater. 150 (2018) 45–49.
[40] J.F. Nie, K. Oh-ishi, X. Gao, K. Hono, Acta Mater. 56 (2008) 6061–6076.
[41] Y. Nie, J. Dai, X. Li, X. Zhang, J. Magnes. Alloy. 9 (2021) 1123–1146.
[42] Z. Yang, M.F. Chisholm, G. Duscher, X. Ma, S.J. Pennycook, Acta Mater. 61 (2013) 350–359.
[43] G.W. Han, I.P. Jones, R.E. Smallman, Acta Mater. 51 (2003) 2731–2742.
[44] T. Tsuru, H. Somekawa, D.C. Chrzan, Acta Mater. 151 (2018) 78–86.
[45] C. He, Z. Li, H. Chen, N. Wilson, J.F. Nie, Nat. Commun. 12 (2021) 722.
[46] X.M. Mei, Q.S. Mei, J.Y. Li, C.L. Li, L. Wan, F. Chen, Z.H. Chen, T. Xu, Y.C. Wang, Y.Y. Tan, J. Mater. Sci. Technol. 125 (2022) 238–251.
[47] Q. Li, Y. Lu, Q. Luo, X. Yang, Y. Yang, J. Tan, Z. Dong, J. Dang, J. Li, Y. Chen, B. Jiang, S. Sun, F. Pan, J. Magnes. Alloy. 9 (2021) 1922–1941.

[48] Y. Pang, D. Sun, Q. Gu, K.-.C. Chou, X. Wang, Q. Li, Cryst. Growth Des. 16 (2016) 2404–2415.
[49] L.S. Mantha, B.E. MacDonald, X. Mu, A. Mazilkin, J. Ivanisenko, H. Hahn, E.J. Lavernia, S. Katnagallu, C. Kübel, Acta Mater. 220 (2021) 117281.
[50] R. Kirchheim, Acta Mater. 50 (2002) 413–429.
[51] Q. Li, X. Lin, Q. Luo, Y.a. Chen, J. Wang, B. Jiang, F. Pan, Int. J. Miner. Metall. Mater. 29 (2022) 32–48.
[52] B.B. Yang, C.Y. Shi, X.J. Ye, J.W. Teng, R.L. Lai, Y.J. Cui, D.K. Guan, H.W. Cui, Y.P. Li, A. Chiba, J. Magnes. Alloy. (2021), doi:10.1016/j.jma.2021.06.008.
[53] I. Toda-Caraballo, E.I. Galindo-Nava, P.E.J. Rivera-Díaz-del-Castillo, Acta Mater. 75 (2014) 287–296.
[54] Q. Yang, S. Lv, Z. Yan, X. Hua, X. Qiu, J. Meng, Mater. Des. 201 (2021) 109482.
[55] Y. Chen, Y. Yang, Z. Feng, B. Huang, X. Luo, W. Zhang, Mater. Charact. 132 (2017) 269–279.
[56] Y. Chen, Y. Yang, Z. Feng, G. Zhao, B. Huang, X. Luo, Y. Zhang, W. Zhang, Mater. Charact. 123 (2017) 189–197.